Emitter Surface Temperature Measurements of a 25-A class Hollow Cathode

IEPC-2022-140

Presented at the 37th International Electric Propulsion Conference
Massachusetts Institute of Technology, Cambridge, MA USA
June 19-23, 2022

Scott J. Hall [1]
HX5, LLC., NASA Glenn Research Center, Cleveland, OH, 44135, USA

Timothy G. Gray[2], Timothy R. Sarver-Verhey [3], and Hani Kamhawi [4]
NASA Glenn Research Center, Cleveland, OH, 44135, USA

The axial emitter surface temperature profile is experimentally characterized for a 25-A class hollow cathode operating across a range of operating conditions. Profiles were measured using a ratio pyrometry diagnostic featuring a fiber optic inserted into the emitter region using a fast motion stage. Emitter temperature is found to increase with increasing discharge current, decreasing flow rate, and increasing magnetic field strength. Across a range of 10 – 29 A, the maximum emitter temperature increased 176 ºC, an order of magnitude more than the changes measured for flow rate or magnetic fields strength. Profiles were generally self-similar across all operating conditions, and the difference between maximum and minimum emitter temperature never surpassed 10%, indicating that this cathode design results in satisfactory emitter utilization across its operating envelope.

I. Motivation and Background

The temperature of the electron emitter of a hollow cathode is strongly related to its service life capability. In barium oxide cathodes, a life-limiting mechanism is barium evaporation, which increases non-linearly with temperature [1]. Emitter temperature can thus be used to estimate cathode lifetime due to this mechanism [2]. Often, emitter temperature is estimated using the cathode orifice plate temperature, which can be measured using contact techniques such as thermocouples or non-contact techniques such as optical pyrometry. Though these approaches are relatively simple and robust, there are two significant shortcomings of using orifice plate temperature to estimate emitter temperature [3]. First, the orifice plate has been shown to differ from the peak emitter surface temperature by more than 50 ºC. Second, there is typically an axial temperature gradient along the emitter surface, at times exceeding 150 ºC [3,4].

Thus, there is a strong interest in characterizing the axial emitter temperature profile of hollow cathodes during operation. One technique for measuring the emitter surface temperature profile was developed by Polk using ratio pyrometry [4], wherein an optical fiber is rapidly inserted into the cathode insert region. This measurement approach offers finer spatial resolution than achievable with thermocouples inserted into the emitter [5] and, through its non-contact nature, avoids concerns about incompatible materials being in contact with the sensitive emitter.

Recently, NASA Glenn Research Center (GRC) built a ratio pyrometry system similar to that of Polk. We used this ratio pyrometry system to make emitter surface temperature measurements across a variety of throttle points of a

[1] Research Engineer, Electric Propulsion Systems Branch.
[2] Research Engineer, Electric Propulsion Systems Branch, timothy.g.gray@nasa.gov.
[3] Research Engineer, Electric Propulsion Systems Branch, timothy.r.verhey@nasa.gov.
[4] Research Engineer, Electric Propulsion Systems Branch, hani.kamhawi-1@nasa.gov.

25-A class cathode called the Mark II, which was developed by NASA GRC for use in the Hall Effect Rocket with Magnetic Shielding (HERMeS) Hall thruster. We measured emitter surface temperature profile as a function of various operating parameters, including discharge current, propellant mass flow rate, and magnetic field strength. These measurements offer insight into how cathode operation and lifetime may be affected by changes in operating condition. This information is critical to making informed decisions on changes to mission operating points.

II. Experimental Apparatus

This experimental campaign used an apparatus similar to that used in many of our previous experiments, and further details of some aspects can be found in References [6–9]. We offer an overview of the apparatus below, as well as details of the emitter temperature diagnostic.

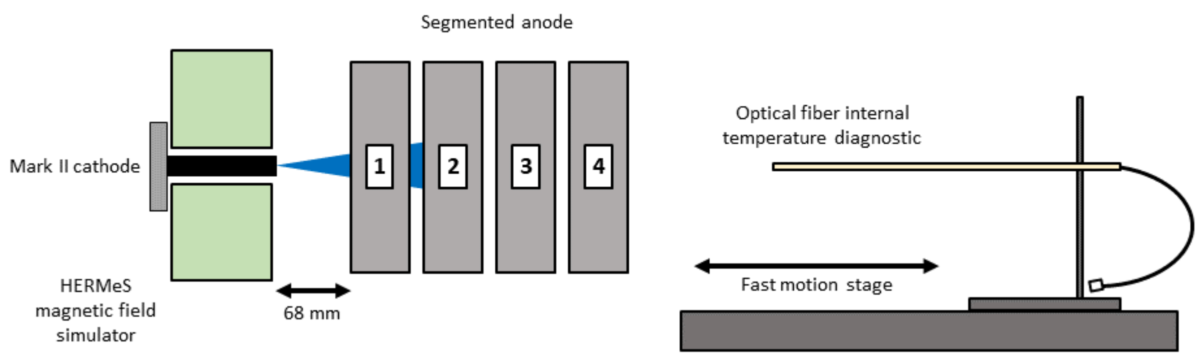

Figure 1. Schematic of experimental apparatus, including Mark II cathode, magnetic field simulator, segmented anode, fast motion stage, and centerline plasma diagnostics.

A. Anode and Cathode

The discharge anode for this experiment was a 254-mm diameter cylindrical anode, divided into four axial segments. The anode was constructed of rolled molybdenum sheet. For all cathode operation here, the anode was operated with all four segments operated by a single discharge power supply. Details of cathode operation with the segmented anode can be found in other publications [6–9].

We used a barium oxide hollow cathode called the Mark II [10]. As noted above, this cathode was developed by NASA GRC for use in the HERMeS Hall thruster. It features brazed joints [11] and draws heritage from a number of previous NASA GRC cathode development efforts [12–18]. The key dimensions of the cathode, including the cathode tube, orifice, and keeper dimensions, all match the laboratory model cathodes used in the TDU-1 and TDU-3 thrusters at NASA GRC [19–24] and for component-level testing [25]. The key dimensions are also similar to the HERMeS cathode developed and tested extensively by JPL [2,26–30], although the JPL cathode utilizes a lanthanum hexaboride emitter. In this experiment, we operated the Mark II across a range of flow rates, discharge currents, and magnetic field strengths spanning its operational envelope. We grounded the cathode to facility ground, a result of the other measurements being made in the same test campaign [8].

B. Magnetic Field Simulator

We constructed a magnetic field simulator that produced similar cathode centerline magnetic field profile and magnitude as the HERMeS Hall thruster. The simulator provided comparable centerline peak magnetic field strengths and centerline profiles as the full HERMeS circuit. For reference, herein when we refer to a magnetic field strength, it is the peak cathode centerline value. For this testing, we operated at a range of magnetic field strengths similar to that used in previous investigations [7].

C. Vacuum Facility and Cathode Support Hardware

This experiment was conducted in Vacuum Facility 1 (VF-1) at NASA GRC. This facility was recently refurbished and outfitted for hollow cathode testing [10]. VF-1 is a 1.5-m diameter, 4.5-m long cylindrical vacuum facility capable of typical base pressures of 1×10^{-7} torr. VF-1 features two 0.9-m diameter cryogenic pumps that provide operating pressures of 9 μTorr-Xe at the nominal Mark II flow rate of 14.7 sccm xenon. We measured facility pressure using an ionization gauge mounted to the facility wall approximately 60 cm behind the cathode exit plane. The gauge was nitrogen-calibrated and corrected for xenon, and we estimate the uncertainty to be ±20% of the reading. Research-grade (99.999% pure) xenon was provided to the cathode using a 50-sccm commercial mass flow controller and electropolished stainless steel tubing.

We collected cathode telemetry using a pair of breakout boxes (one for the segmented anode and one for the remainder of cathode power) and a multiplexed data acquisition system. Cathode orifice plate temperature was measured using a type-R thermocouple spot-welded to the edge of the orifice plate. Uncertainty of the thermocouple reading is estimated as ±2.5 ºC.

D. Emitter Temperature Diagnostic

The emitter temperature diagnostic (ETD) at GRC is similar to that developed by Polk and described in Reference [4]. The system consists of a sapphire fiber optic probe rapidly inserted into the emitter region. The fiber probe tip is polished to 45º to collect light from the emitter surface. The collected light is split into two beams that are separately band pass filtered at 1200 nm and 1500 nm, respectively, and measured using infrared detectors. The ratio of these two signals is then used to calculate the temperature of the emitter surface.

Our implementation differs from that described in Reference [4] in two important ways. First, the fiber optic probe enters the cathode through the front, traversing through the anode and into the insert region. Second, instead of relying on the cathode heater as a calibration source, a specially designed calibration oven was designed and built out of graphite. More details on both aspects are provided below.

1. Configuration

The optical fiber probe was mounted on a fast motion stage and aligned to cathode centerline. The stage rapidly inserted and retracted the fiber optic at 500 mm/s. The encoder signal from the motion stage was read alongside the signal from each of the IR detectors by an 8-channel, 16-bit digital oscilloscope. We configured the fast motion stage position encoder to trigger every 1 mm of stage movement, and the oscilloscope captured approximately 2500 points per 1 mm of stage travel. In post processing, these signals were binned and averaged every 1 mm, providing spatial profiles along the emitter length.

2. Calibration

We used a custom graphite calibration oven to perform *in situ* calibration of the diagnostic (Figure 2). This oven consisted of a graphite slug mimicking the geometry of the cathode insert, wrapped in a resistive heater similar to that used in the cathode, and enclosed in an outer, keeper-like graphite shroud. The graphite slug had four pockets for Type-R thermocouples. One thermocouple was located 25% along the axial length of the slug, one at 75%, and two at 50%. These four thermocouples were read by the same multiplexing data acquisition system and have the same uncertainty of ±2.5 ºC as the cathode orifice plate thermocouple. The oven was mounted to a linear motion stage such that it could be moved onto cathode centerline for use and then removed to be out of line-of-sight of the cathode during cathode operation.

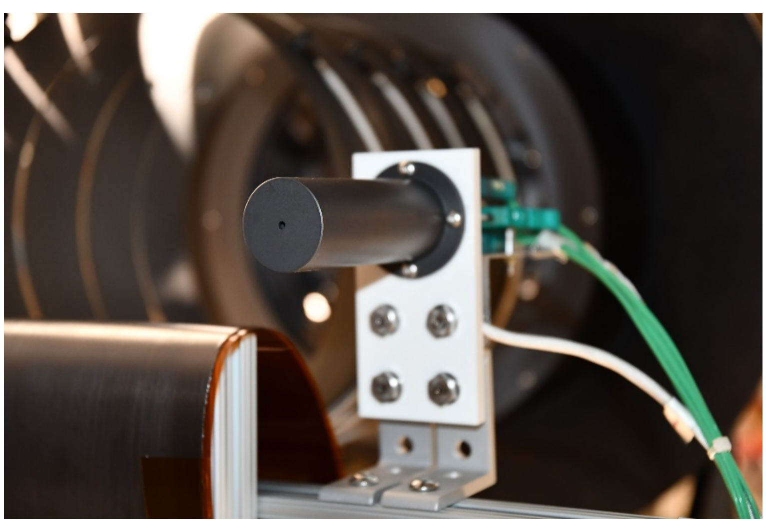

Figure 2. The ETD calibration oven.

At the end of each test day, after the cathode was shut off, the ETD system was calibrated. The oven was initially heated at 5.5 A of heater current for 15 minutes, which allowed the four thermocouples to reach thermal steady state. The ETD probe was then inserted into the oven to the 50% axial length position, a measurement was taken, and the probe was removed. The heater current was then increased by 0.5 A and the oven allowed to heat for 5 minutes, then another measurement was taken. With this approach, we built a calibration curve of the probe response as a function of slug temperature. The oven can produce temperatures from 850 ºC to 1200 ºC, sufficient to bracket the temperature range of the Mark II cathode. The standard deviation of the four thermocouples in the oven was found to be 4.8 ºC, and the response of the oven was repeatable to within 10 ºC day-to-day.

3. Measurement Technique

During cathode operation, the ETD probe was shielded behind a graphite plate to keep it out of the plasma until a measurement was taken. We allowed the cathode to reach thermal equilibrium on the orifice plate thermocouple prior to making a measurement at any given throttle condition. To make a measurement, the graphite shield was removed and the fast motion stage was actuated. In post processing, we performed the bin-and-averaging of each signal as described above, then took the ratio of the two signals and applied the calibration from the oven. This resulted in temperature profiles as a function of axial position. Following the assessment by Polk [4], we calculate that the uncertainty in our temperature measurements is ± 5.5 ºC.

III. Results

We measured emitter temperature profiles as a function of varying discharge current, mass flow rate, and magnetic field strength. We present these results as profiles as a function of normalized axial location upstream of the orifice plate, z/L_{emit}. This normalized position is zero at the orifice plate and negative moving upstream (into the cathode). The above-noted uncertainty on the measurements is reflected in each plot as an error band around a single profile for clarity.

Figure 3 shows profiles as a function of discharge currents from 10 A to 29 A at the nominal cathode flow rate of 14.7 sccm xenon and the highest magnetic field strength, 325 G. Emitter temperature increases with increasing discharge current, as expected. The profile appears to remain self-similar across the range of discharge currents tested, with the entire emitter temperature increasing monotonically with increasing current. Across our range of measurements, the average change in maximum emitter temperature was 9.6 ± 1.4 ºC/A. The variation in maximum emitter temperature between 10 A and 29 A is 176 ºC.

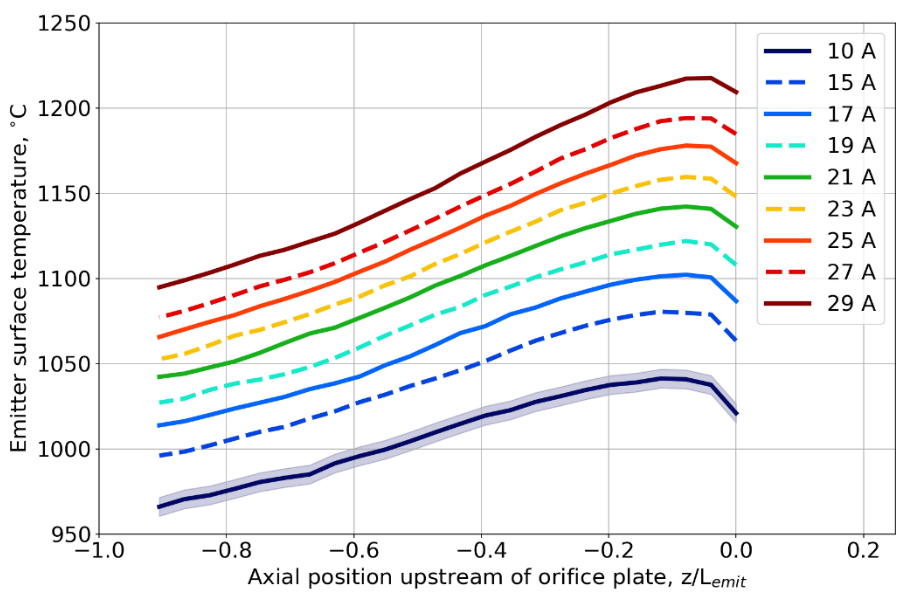

Figure 3. Axial emitter temperature profiles for varying discharge current at 14.7 sccm xenon and 325 G magnetic field strength. Uncertainty in the measurement is shown in the error band on the 10 A condition.

Next, we show emitter temperature profiles as a function of flow rate in Figure 4. Emitter temperature generally decreases with flow rate, but the change is not monotonic. The profiles for 40 sccm, 29 sccm, and 25 sccm are indistinguishable. The variation in maximum emitter temperature across all flow rates tested is only 17 ºC, which highlights the relatively small impact of flow rate as compared to discharge current.

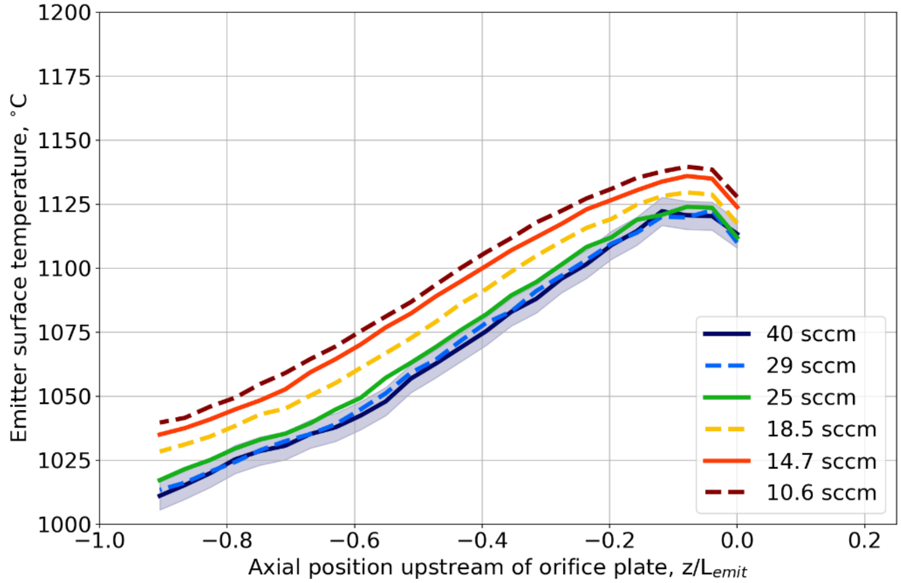

Figure 4. Axial emitter temperature profiles for varying flow rate at 20.8 A discharge current and 325 G magnetic field strength. Uncertainty in the measurement is shown in the error band on the 40 sccm condition.

Finally, we turn to variation magnetic field strength in Figure 5. Emitter temperature increased with increasing magnetic field strength. The maximum temperature increased monotonically by a total of 16 ºC between the 0 G and 325 G conditions. The change in temperature was more significant near the orifice plate and the location of maximum temperature than it was near the upstream end of the emitter ($z/L_{emit} = -1$), where the increase was only 7 ºC from 0 G to 325 G. The relative effect of magnetic field strength is similar to that of flow rate in magnitude.

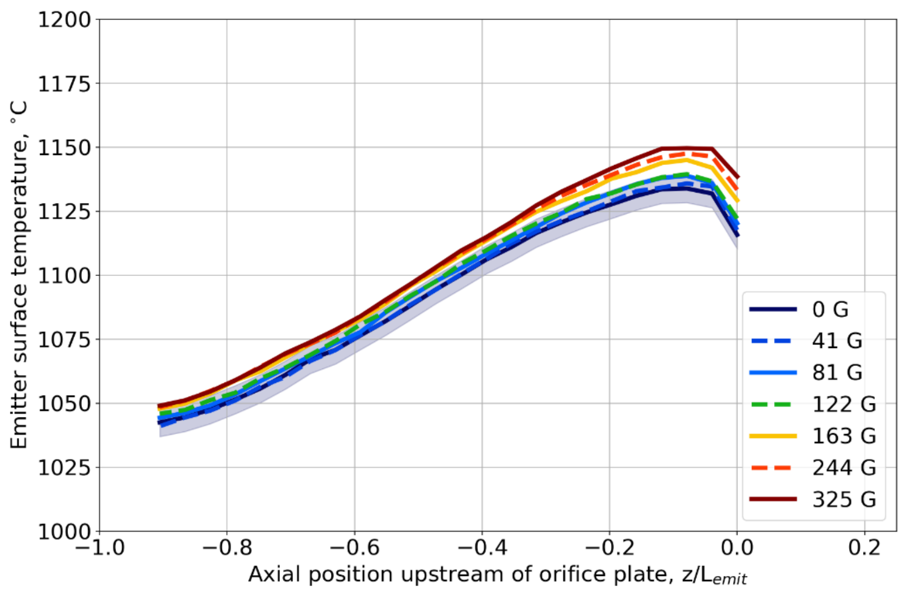

Figure 5. Axial emitter temperature profiles for varying magnetic field strength at 20.8 A discharge current and 14.7 sccm flow rate. Uncertainty in the measurement is shown in the error band on the 0 G condition.

IV. Discussion

A. Change in Profile

The plots presented in Section III above highlight the variation in magnitude well, and illustrate that there is not large-scale change in the temperature profile with changes in the cathode operating condition. However, the nature of those plots makes identifying smaller changes in profile difficult to discern. To highlight these smaller changes, Figure 6 shows normalized profiles for each operating parameter. Each individual profile has been normalized to its maximum temperature.

Variation with discharge current is shown in the left-hand plot. With increasing discharge current, we find that the portion of the emitter upstream of the maximum (z/L_{emit} more negative) operates relatively cooler. This results in a more even temperature distribution at lower discharge current. At 10 A discharge current, the farthest upstream point is 93% of the maximum emitter temperature, whereas at 29 A the same point is 90% the maximum emitter temperature. Additionally, the location of maximum temperature moves slightly downstream (closer to the orifice plate), shifting from $z/L_{emit} = -0.12$ at 10 A to $z/L_{emit} = -0.04$ at 29 A.

In the middle plot, we find that increasing flow rate similarly drives the upstream portion of the emitter to lower relative temperatures. However, the variation in profile is smaller, changing from 91% at 10.6 sccm to 92% at 40 sccm. Unlike changing discharge current, changing flow rate does not appear to affect the location of maximum emitter temperature.

Normalized profiles for varying magnetic field strength are in the right-hand plot, which illustrate that increasing magnetic field strength results in decreased relative temperature on the upstream portion of the emitter. The changes in profile are very similar to those observed with flow rate, with a similar variation between the lowest and highest condition. Also similar to flow rate—and different from discharge current—magnetic field strength has no impact on the location of the maximum emitter temperature.

By presenting the profiles in this way, another result is clear. Across all conditions tested, the temperature variation across the emitter never exceeded 10%. This is evidence that the emitter length is being well-utilized for current emission, a key aspect to long-life cathode design.

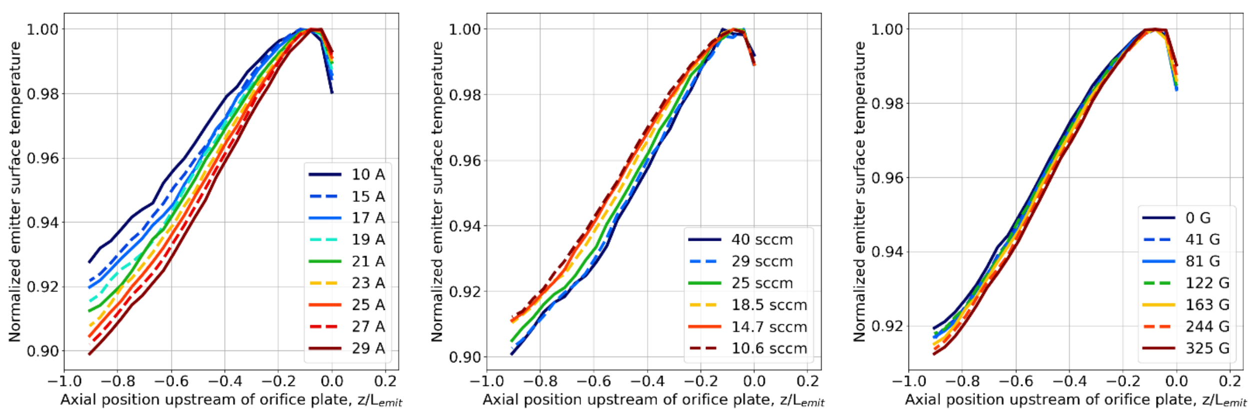

Figure 6. Normalized axial emitter temperature profiles for all conditions tested.

B. Comparison to Orifice Plate Thermocouple

Thermocouples mounted to the cathode orifice plate are often used as a simple means of characterizing the cathode operating temperature. Because our cathode was outfitted with an orifice plate thermocouple that we recorded during ETD operation, we are able to compare the measurements to understand whether the two techniques capture similar magnitudes or trends, assessing the validity of using an orifice plate thermocouple where invasive internal measurements cannot be performed.

We present the maximum emitter temperature and the orifice plate thermocouple measurement as a function of each of the three operating variables we tested in Figure 7. It is immediately apparent that the orifice plate thermocouple reports a temperature significantly lower than the maximum emitter temperature measurement, but that offset is approximately constant across all operating conditions. The difference is not surprising considering the shape of the profiles presented above, which showed the maximum emitter temperature upstream of the orifice plate. Given this profile, we would expect the orifice plate to be cooler than the maximum emitter temperature, exactly as observed.

However, though the orifice plate thermocouple does not offer a direct measurement of the maximum emitter temperature, it does accurately capture the trends of maximum emitter temperature with increasing discharge current, mass flow rate, and magnetic field strength. Across all conditions, the maximum emitter temperature was higher than the orifice plate thermocouple reading by 134 ºC with a standard deviation of 10 ºC, with no trend with temperature. We do expect that the offset between the two measurement techniques will depend on the temperature profile along the emitter—that is, the location of the maximum emitter temperature relative to the orifice plate, as well as the slope of the temperature—but these measurements suggest that an orifice plate thermocouple offers a means to capture the trends of emitter temperature with varying operating parameters.

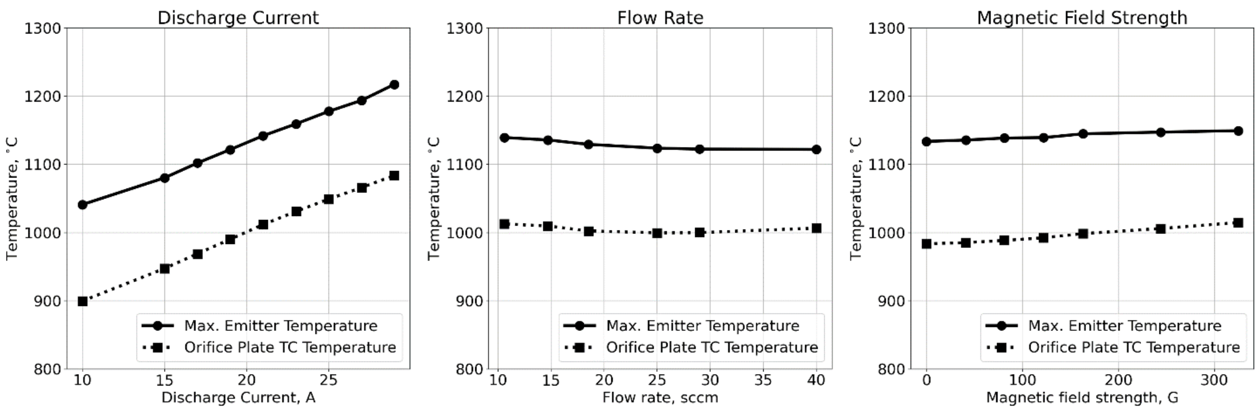

Figure 7. Maximum emitter temperature compared to orifice plate thermocouple measurement for all operating conditions tested.

V. Conclusions

An emitter temperature diagnostic was built at NASA GRC that can measure the emitter temperature profile of operational hollow cathodes. The diagnostic uses a sapphire optical fiber that is rapidly inserted through the orifice of the cathode using a reciprocating motion stage. The signal from the fiber is band-pass filtered to 1200 nm and 1500 nm, and the ratio of these two signals is used to calculate the surface temperature via ratio pyrometry. The diagnostic uses a dedicated graphite calibration oven for *in situ* calibration. The oven is outfitted with four thermocouples and a coaxial heater and produces temperatures from 850 ºC to 1200 ºC.

We used the diagnostic to characterize the emitter temperature profiles of a 25-A class hollow cathode as a function of discharge current, flow rate, and applied magnetic field strength. We found that discharge current affected emitter temperature most strongly across the range tested, with a sensitivity of approximately 10 ºC/A and a total increase of 176 ºC from 10 A to 29 A. Increasing flow rate resulted in a decrease in emitter temperature of approximately 17 ºC between flow rates of 10.6 sccm and 40 sccm. However, unlike discharge current, this change was non-linear, as the three highest flow rates (25, 29, and 40 sccm) had nearly indistinguishable temperature profiles and maximum temperatures. Increasing magnetic field strength resulted in monotonically increasing emitter temperature, with a total increase of approximately 16 ºC between the 0 G and 325 G conditions.

By normalizing the profiles, we highlighted subtle changes in their shape for each parameter. This showed that increasing discharge current produces a steeper gradient in temperature and causes the location of maximum temperature to be closer to the orifice plate. Increasing magnetic field strength and flow rate both caused steeper gradients in temperature but no change in the location of maximum temperature. For all conditions tested, the difference between the maximum and minimum temperature was 10% or less, indicating strong emitter utilization.

We also compared the maximum emitter temperature from the diagnostic to the temperature measured by a thermocouple mounted to the orifice plate of the cathode. Though the maximum emitter temperature exceeded the orifice plate thermocouple by an average of 135 ºC, we found that both diagnostics reported the same trends with each operating parameter. This indicates that although an orifice plate thermocouple may not offer an absolute measure of maximum emitter temperature, it will capture the trends in emitter temperature with varying parameters, making it an effective diagnostic in certain situations where the invasive nature of the ETD is undesirable.

VI. Acknowledgments

This work was supported by NASA's Space Technology Mission Directorate through the Solar Electric Propulsion project. We would also like to thank Peter J. Minidis, Luke T. Sorrelle, Thomas A. Bollinger, Matthew T. Daugherty, Kevin A. McCormick, and James A. Schneider of the GRC Space Environments Test Branch for the design and construction of the test hardware and equipment, and operation of the vacuum facility. We also gratefully acknowledge

Nathaniel Wirgau of the Plasma Science and Technology Laboratory at the University of Michigan for his work in the design and construction of the emitter temperature diagnostic.

VII. References

[1] Sarver-Verhey, T. R. Scenario for Hollow Cathode End-of-Life. Kitakyushu, Japan, 1999.
[2] Ortega, A. L., Mikellides, I. G., and Goebel, D. M. Numerical Simulations for Life Assessments of the BaO and LaB6 Cathode Options in the Hall Effect Rocket with Magnetic Shielding (HERMeS). Presented at the 35th International Electric Propulsion Conference, Atlanta, GA, 2017.
[3] Polk, J., Marrese, C., Dang, L., Johnson, L., and Thornber, B. Temperature Distributions in Hollow Cathode Emitters. Presented at the 40th AIAA/ASME/SAE/ASEE Joint Propulsion Conference and Exhibit, AIAA-2004-4116, Ft. Lauderdale, FL, 2004.
[4] Polk, J. E., Marrese-Reading, C. M., Thornber, B., Dang, L., Johnson, L. K., and Katz, I. "Scanning Optical Pyrometer for Measuring Temperatures in Hollow Cathodes." *Review of Scientific Instruments*, Vol. 78, No. 9, 2007, p. 093101.
[5] Guerrero, P., Polk, J. E., Lobbia, R. B., and Mikellides, I. G. Determination of the Work Function Distribution of a LaB6 Hollow Cathode Based on Plasma Potential Measurement and 2D Plasma Numerical Simulation. 2018.
[6] Hall, S. J., Gray, T. G., Yim, J. T., Choi, M., Mooney, M. M., Sarver-Verhey, T. R., and Kamhawi, H. The Effect of Anode Position on Operation of a 25-A Class Hollow Cathode. Presented at the 36th International Electric Propulsion Conference, IEPC-2019-299, Vienna, Austria, 2019.
[7] Hall, S. J., Gray, T. G., Yim, J. T., Choi, M., Mooney, M. M., Sarver-Verhey, T. R., and Kamhawi, H. The Effect of a Hall Thruster-like Magnetic Field on Operation of a 25-A Class Hollow Cathode. Presented at the 36th International Electric Propulsion Conference, IEPC-2019-300, Vienna, Austria, 2019.
[8] Hall, S. J., Gray, T. G., Sarver-Verhey, T. R., and Kamhawi, H. The Effect of Anode Configuration on the Plasma Plume of a 25-A Class Hollow Cathode. Presented at the 2021 AIAA Propulsion and Energy Forum, Paper AIAA-2021-3376, Virtual, 2021.
[9] Hall, S. J., Gray, T. G., Yim, J. T., Choi, M., Sarver-Verhey, T. R., and Kamhawi, H. "The Effect of Facility Background Pressure on Hollow Cathode Operation." *Journal of Applied Physics*, Vol. 130, No. 11, 2021, p. 113302.
[10] Hall, S. J., Sarver-Verhey, T. R., Frieman, J. D., Kamhawi, H., and Myers, J. L. Preparation for Hollow Cathode Testing for the Advanced Electric Propulsion System at NASA Glenn Research Center. Presented at the 2018 Joint Propulsion Conference, AIAA-2018-4425, Cincinnati, OH, 2018.
[11] Hofer, R. R., Polk, J. E., Sekerak, M. J., Mikellides, I. G., Kamhawi, H., Sarver-Verhey, T. R., Herman, D. A., and Williams, G. The 12.5 KW Hall Effect Rocket with Magnetic Shielding (HERMeS) for the Asteroid Redirect Robotic Mission. Presented at the 52nd AIAA/SAE/ASEE Joint Propulsion Conference, AIAA-2016-4825, 2016.
[12] Sarver-Verhey, T. R. 28,000 Hour Xenon Hollow Cathode Life Test Results. Presented at the 25th International Electric Propulsion Conference, Cleveland, OH, 1997.
[13] Sarver-Verhey, T. R. Destructive Evaluation of a Xenon Hollow Cathode After a 28,000 Hour Life Test. Presented at the 34th AIAA/ASME/SAE/ASEE Joint Propulsion Conference and Exhibit, Cleveland, OH, 1998.
[14] Anderson, J. R., Goodfellow, K. D., Polk, J. E., Rawlin, V. K., and Sovey, J. S. Performance Characteristics of the NSTAR Ion Thruster during an On-Going Long Duration Ground Test. In *2000 IEEE Aerospace Conference Proceedings*, No. 4, 2000, pp. 99–122.
[15] Patterson, M. J., Foster, J. E., Haag, T. W., Rawlin, V. K., Soulas, G. C., and Roman, R. F. NEXT: NASA's Evolutionary Xenon Thruster. Presented at the 39th AIAA Joint Propulsion Conference, Indianapolis, IN, 2002.
[16] Carpenter, C. B., and Patterson, M. J. High-Current Hollow Cathode Development. Presented at the 27th International Electric Propulsion Conference, Pasadena, CA, 2001.
[17] Thomas, R. E., Kamhawi, H., and Williams, Jr., G. J. High Current Hollow Cathode Plasma Plume Measurements. Presented at the 33rd International Electric Propulsion Conference, Washington D.C., 2013.
[18] Kamhawi, H., and VanNoord, J. Development and Testing of High Current Hollow Cathodes for High Power Hall Thrusters. Presented at the 48th AIAA/ASME/SAE/ASEE Joint Propulsion Conference and Exhibit, AIAA-2012-4080, Atlanta, GA, 2012.
[19] Kamhawi, H., Haag, T., Huang, W., Herman, D. A., Thomas, R., Shastry, R., Yim, J., Chang, L., Clayman, L., Verhey, T., and others. Performance and Facility Background Pressure Characterization Tests of NASA's 12.5-KW Hall Effect Rocket with Magnetic Shielding Thruster. Presented at the 34th International Electric Propulsion Conference, Kobe-Hyogo, Japan, 2015.
[20] Kamhawi, H., Haag, T., Huang, W., Yim, J., Herman, D. A., Peterson, P. Y., Williams, G., Gilland, J., Hofer, R. R., and Mikellides, I. G. Performance, Facility Pressure Effects, and Stability Characterization Tests of NASA's 12.5-KW Hall Effect Rocket with Magnetic Shielding Thruster. Presented at the 52nd AIAA/SAE/ASEE Joint Propulsion Conference, AIAA-2016-4826, Salt Lake City, UT, 2016.
[21] Kamhawi, H., Huang, W., Gilland, J. H., Haag, T. W., Mackey, J., Yim, J., Pinero, L., Williams, G., Peterson, P., and Herman, D. Performance, Stability, and Plume Characterization of the HERMeS Thruster with Boron Nitride Silica Composite Discharge Channel. Presented at the 35th International Electric Propulsion Conference, IEPC-2017-392, Atlanta, GA, 2017.
[22] Williams, G., Gilland, J. H., Peterson, P. Y., Kamhawi, H., Huang, W., Swiatek, M., Joppeck, C., Yim, J., and Haag, T.

2000-Hour Wear-Testing of the HERMeS Thruster. Presented at the 52nd AIAA/SAE/ASEE Joint Propulsion Conference, AIAA-2016-5025, Salt Lake City, UT, 2016.
[23] Williams Jr, G. J., Kamhawi, H., Choi, M., Haag, T. W., Huang, W., Herman, D. A., Gilland, J. H., and Peterson, P. Y. Wear Trends of the HERMeS Thruster as a Function of Throttle Point. Presented at the 35th International Electric Propulsion Conference, IEPC-2017-207, Atlanta, GA, 2019.
[24] Peterson, P. Y., Kamhawi, H., Huang, W., Williams, G., Gilland, J. H., Yim, J., Hofer, R. R., and Herman, D. A. NASA's HERMeS Hall Thruster Electrical Configuration Characterization. Presented at the 52nd AIAA/SAE/ASEE Joint Propulsion Conference, AIAA-2016-5027, Salt Lake City, UT, 2016.
[25] Sarver-Verhey, T. R., Kamhawi, H., Goebel, D. M., Polk, J. E., Peterson, P. Y., and Robinson, D. A. Hollow Cathode Assembly Development for the HERMeS Hall Thruster. Presented at the 52nd Joint Propulsion Conference, Salt Lake City, UT, 2016.
[26] Yanes, N., Jorns, B., Friss, A., Polk, J. E., Guerrero, P., and Austin, J. M. Ion Acoustic Turbulence and Ion Energy Measurements in the Plume of the HERMeS Thruster Hollow Cathode. Presented at the 52nd Joint Propulsion Conference and Exhibit, AIAA-2016-5088, Salt Lake City, UT, 2016.
[27] Goebel, D. M., and Polk, J. E. Lanthanum Hexaboride Hollow Cathode for the Asteroid Redirect Robotic Mission 12.5 KW Hall Thruster. Presented at the 34th International Electric Propulsion Conference, IEPC-2015-043, Kobe-Hyogo, Japan, 2015.
[28] Polk, J. E., Goebel, D. M., and Guerrero, P. Thermal Characteristics of Lanthanum Hexaboride Hollow Cathodes. Presented at the 34th International Electric Propulsion Conference, IEPC-2015-044, Kobe-Hyogo, Japan, 2015.
[29] Goebel, D. M., Becatti, G., Polk, J. E., and Guerrero, P. Life Model for Lanthanum Hexaboride Hollow Cathodes for High-Power Hall Thrusters. Presented at the 35th International Electric Propulsion Conference, IEPC-2017-276, Atlanta, GA, 2017.
[30] Polk, J. E., Lobbia, R. B., Barriault, A., Guerrero, P., Mikellides, I., and Ortega, A. L. Inner Front Pole Cover Erosion in the 12.5 KW HERMeS Hall Thruster Over a Range of Operating Conditions. Presented at the 35th International Electric Propulsion Conference, Atlanta, GA, 2017.